RSC Advances

ROYAL SOCIETY OF CHEMISTRY

www.rsc.org/advances

RSC Advances

RSCPublishing

ARTICLE

α-Fe_2O_3 Nanopillar Arrays Fabricated by Electron Beam Evaporation for the photoassisted degradation of dye with H_2O_2

Cite this: DOI: 10.1039/x0xx00000x

Received 00th January 2012,
Accepted 00th January 2012

DOI: 10.1039/x0xx00000x

www.rsc.org/

Shuang Shuang,[a] Ruitao Lv,[b] Zheng Xie,[a, c] Weipeng Wang,[a] Xiaoyang Cui, [a] Shuai Ning [a] and Zhengjun Zhang [b]*

Vertically aligned α-Fe_2O_3 nanopillar arrays (NPAs) were fabricated by thermally oxidizing Fe NPAs on Si, quartz and F-doped SnO_2 (FTO) substrates prepared by glancing angle e-beam deposition (GLAD). The photocatalytic activity of these NPAs was evaluated by measuring the photodegradation of crystal violet (CV) and methyl orange (MO) in presence of H_2O_2 under visible light irradiation. Moreover, the photoelectrochemical (PEC) performance was also studied. Typically the sample oxidized at 400 ^oC exhibits both the highest degradation efficiency and photocurrent density compared with those oxidized at other temperatures (e.g. 300 ^oC, 350 ^oC, 450 ^oC, 500 ^oC). This phenomenon might be attributed to a trade-off in between two opposite effects. On the one hand, with the increase of the oxidation temperature, the improvement of NPAs' crystallinity will enhance the photocatalytic performance accordingly. On the other hand, increasing oxidation temperature may cause the reduction of oxygen vacancies on the NPAs' surface, which are actually regarded as photoreaction active sites. This thus will degrade the photocatalytic performance.

Introduction

Since the first observation of photo electrochemical (PEC) splitting of water over TiO_2 electrodes by Fujishima and Honda in 1972[1], semiconductor-based photocatalysis has attracted increasing attention of researchers, as it provides an effective way to convert solar energy into chemical and electrical energy, and can be used in a diversity of fields, such as decomposing organic pollutants, hydrogen generation, etc[2]. However, as a wide band gap (~3.0 eV) semiconductor, TiO_2 works only in the UV region which is only ~4% of the incident solar radiation[3]. In order to fully utilize the solar energy, efficient semiconductors that work in the visible light region as well as the UV region are highly demanded. However, developing brand-new high-performance catalysts that can efficiently extend photocatalytic activity into visible spectral region still remains a big challenge. Actually, in addition to the effort in developing novel photocatalysts, traditional materials can also be modified by various strategies to achieve high catalytic activity under visible light irradiation.

Hematite (α-Fe_2O_3), an abundant environmentally friendly n-type semiconductor, has been widely used as catalysts[4], pigment[5], gas sensors[6]. It has a band gap of ~ 2.1 eV, and works in the visible light region with a high theoretical solar-to-hydrogen efficiency of ~17% and good stability against photocorrosion[7]. Therefore, α-Fe_2O_3 has attracted tremendous interests in recent years[8-15]. However, a drawback of α-Fe_2O_3 catalyst is the short hole diffusion length (2~4 nm) due to its poor minority charge carrier mobility (0.2 $cm^2 \bullet V^{-1} \bullet s^{-1}$), which results in a high recombination rate of electrons and holes, a very short excited state lifetime (~10 ps), and poor electrical conductivity[16, 17]. To address or to overcome this issue, a lot of efforts have been paid to synthesize nanostructures of Hematite, such as nanotubes, nanoparticles, nanocubes, nanowires, nanofibers, nanorods, and hierarchical structures[8-15, 18]. Besides morphology control, other ways like doping, constructing heterojunctions, surface functionalization of nanostructures, etc., can also be used to optimize its photocatalytic performance[9, 19-22].

Photocatalysts in previous reports are usually in the form of powders, which is hard to handle and collect. Here we report the synthesis of vertically aligned hematite nanopillar arrays on specific substrates to form self-standing structures, which are much easier to recycle. Furthermore, they do prevent the occurrence of secondary pollution which means more than recycles. The α-Fe_2O_3 arrays are fabricated by thermally oxidizing Fe nanopillars using a glancing angle deposition (GLAD) technique. The PEC and degradation performance under visible light radiation are evaluated. The influence of the oxidization temperature on the growth of hematite nanopillars and their catalytic performance are also investigated.

Experimental Methods

Fabrication of α-Fe_2O_3 Nanopillar Arrays

Vertically aligned Fe nanopillars were deposited by the e-beam GLAD technique onto three different substrates as below: 1) planar silicon substrates with (001) orientation for material characterization, 2) quartz substrates for degradation reaction, and 3) F-doped SnO_2 (FTO) substrates (20 Ω per square) for PEC test. All the substrates were ultrasonically cleaned in sequence in acetone, ethanol and deionized (DI) water baths for 10 min respectively. Prior to the deposition, the chamber was evacuated to a vacuum level above 1×10^{-8} Torr. During deposition, the vapor flux incident angle was set to ~86° off the surface normal to the substrates, rotating at a speed of 10 RPM. The deposition rate (~0.75 nm•s^{-1}) and the height of the nanopillars were monitored by a quartz crystal microbalance. After deposition, the samples were subjected to the oxidation process in a quartz tube furnace for 1 hr at a ramp of 2 °C min-1 under ambient conditions to temperatures of 300, 350, 400, 450 and 500 °C, respectively. For comparison with powder sample, we prepared α-Fe_2O_3 sol using Fe_2O_3 powders. Then we paint it onto the same SiO_2 substrate to test properties.

Characterization and Measurement

The morphology and structure of the samples were examined by field-emission scanning electron microscope (FESEM, JEOL-7001F), high-resolution transmission electron microscope (HRTEM, JEOL-2011) and Raman spectroscopy (LABRAM HR800, excitation wavelength of 633 nm), respectively. The chemical structure of the samples was analyzed by x-ray photon electron spectrometer (XPS, Perkin Elmer PHI 5300), and the binding energy was calibrated with the reference to the C 1s peak centered at 284.6 eV. The optical properties of the samples were examined by a UV–vis spectrometer (Perkin Elmer Lambda 35) in a wavelength range of 200 to 900 nm at room temperature.

The steady sate current density (*j–V*) and electrochemical impedance spectroscopy (EIS) measurements were carried out by an electrochemistry workstation (CHI 660D, Chenhua instrument). The nanostructured films were used as the working electrode, an Ag/AgCl electrode (saturated KCl) and Pt sheet were used as the reference and counter electrodes, respectively. The working electrode was illuminated with a 300 W Xe lamp. An ultraviolet filter was placed between the light source and the quartz cell to cut off the UV light in wavelength <420 nm. Photocurrent densities were measured in the light on-off process with a pulse of 30 s under visible light illumination (200 mW•cm^{-2}) at 0.4 V bias vs Ag/AgCl electrode.

The photocatalytic activity of the hematite nanopillar arrays was evaluated by the photodegradation of crystal violet (CV) and methyl orange (MO) photodegradation with the light source of 300 W Xe lamp at ambient temperature. The sample on quartz substrate (15 mm×15 mm) was placed in a quartz cell containing 5 mL of CV (5 μM) and MO (5 μM). Prior to light irradiation, the photocatalyst was immersed into solution in the dark room for 30 min to reach an adsorption/desorption equilibrium, then 12 μL of 30 wt% H_2O_2 was added to the solution, and the Xe lamp was turned on for different time spans. After that, the UV-vis absorbance spectra of the dye aqueous solution were obtained to measure the dye concentration after photodegradation.

Results and Discussion

Figure 1(a), 1(c), 1(e) and 1(f) show typical top-view SEM images of the as-deposited film and those oxidized at 300, 400 and 500 °C respectively. Figure 1(b) and 1(d) show typical side-view SEM images of the as-deposited film and the film oxidized at 300 °C, respectively. It can be seen that the as-deposited film consists of vertically aligned Fe nanopillars, with a diameter of ~30 nm and a length of ~200 nm. After thermal oxidation, as shown by Figure 1(c) and 1(d), the diameter of the nanopillars was increased to ~55 nm, and they touched with each other slightly. No obvious difference is observed among samples oxidized at 300, 400 and 500 °C.

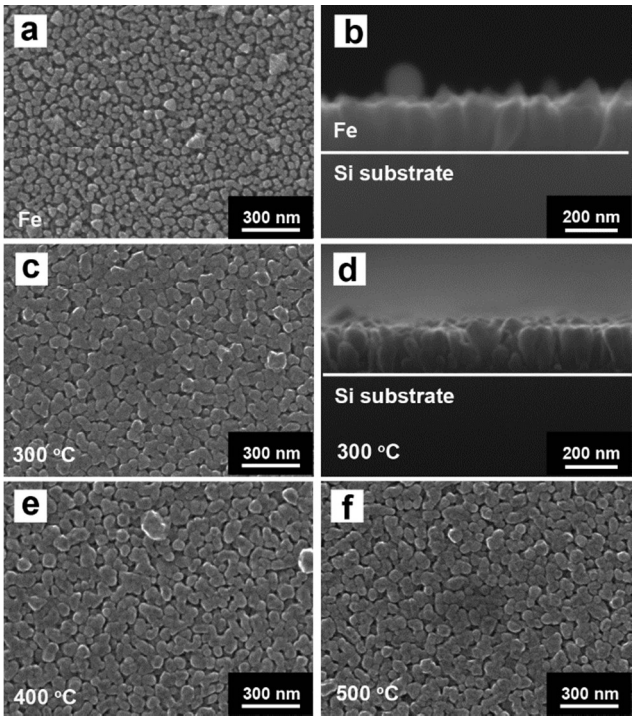

Figure 1. SEM images of the different samples: (a) Fe nanopillar film; (b) cross-section of Fe nanopillar film; (c) α-Fe_2O_3 films oxidized at 300 °C; (d) cross-section of sample oxidized at 300 °C ; (e) α-Fe_2O_3 films oxidized at 400 °C; (f) α-Fe_2O_3 films oxidized at 500 °C.

Figure 2 shows the XRD patterns of the as-prepared samples. The XRD pattern of the Fe sample is well matched with the standard spectrum of Fe (JCPDS 50-1275). When the oxidation temperature are 300 and 350 °C, the main phase is α-Fe_2O_3 (JCPDS 33-0664) with a little diffraction peak located at 30.1 °, which can be ascribed to the (220) plane of γ-Fe_2O_3 (JCPDS 39-1346). This indicates that a few amount of γ-Fe_2O_3 co-existing in the sample. When the annealing temperature is higher than 350 °C, the phase will be totally α-Fe_2O_3.

Figure 3 shows the Raman spectra of the as-deposited film and films oxidized at temperatures ranging from 300 to 500 °C, measured at room-temperature. It can be seen that, all samples oxidized at temperatures above 300 °C demonstrate the characteristic peaks corresponding to α-Fe_2O_3, i.e. peaks at 226 and 493 cm^{-1} of the A_{1g} mode, and peaks at 295, 411 and 610 cm^{-1} of the E_g mode[23, 24]. The peak centered at 1318 cm^{-1} may be caused by the two-magnon scattering due to the interaction between two magnons created on antiparallel close spin sites. It is noticed that the films oxidized at low temperatures (e.g. 300 °C, 350 °C) exhibited broader and lower intensity Raman peaks, whilst the films oxidized at higher temperatures exhibited sharper and higher intense Raman peaks because of better crystallinity[25].

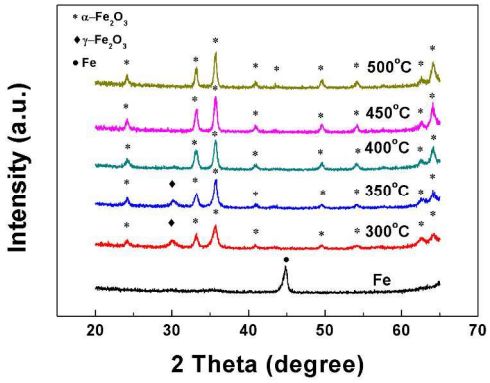

Figure 2. XRD spectra of the as-deposited Fe films and oxidized samples at different temperatures

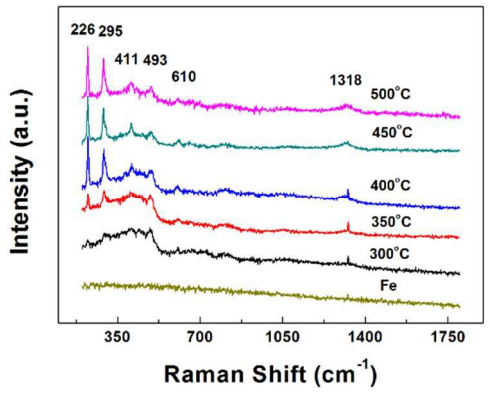

Figure 3. Raman spectra of the as-deposited Fe films and oxidized samples at different temperatures

Figure 4 shows XPS spectra of the films oxidized at 300, 400 and 500 °C, where the binding energies were corrected by referencing the C 1s line to 284.6 eV. The peaks located at ~710 and ~724 eV are in good agreement with the Fe $2p^{3/2}$ and Fe $2p^{1/2}$ binding energy of Fe^{3+} [26]. The little shakeup satellite structure between two main peaks is the fingerprint of the electronic structure of Fe^{3+} [27]. Based on Raman and XPS analysis, it can be known that Fe nanopillars are oxidized into hematite nanopillars by the oxidization treatment at 300-500 °C.

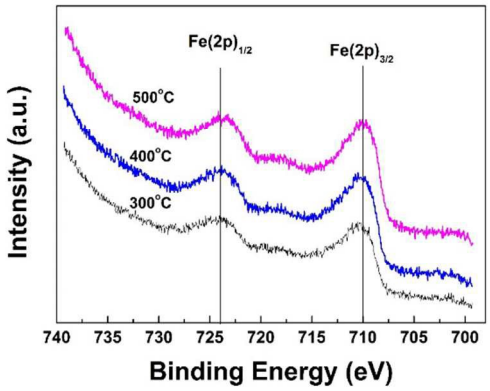

Figure 4. Fe 2p XPS spectra of samples oxidized at 300, 400 and 500 °C, respectively

The morphology and structure of individual nanopillars after oxidization were also investigated by TEM analysis. Figure 5(a)-(d) shows typical low-magnification and high-magnification HRTEM images of the nanopillars oxidized at 300 and 400 °C, respectively. Insets of (b) and (d) show their corresponding selected-area electron diffraction (SAED) patterns. Patterns are of 300 and 400 °C oxidation temperature. We check α-Fe_2O_3 PDF card with some indices of crystal face to confirm its phase, marked in figures. The SAED rings of the sample oxidized at 400 °C correspond to the (113), (110), (104), (012), and (101) planes of α-Fe_2O_3, respectively. It can be seen that the nanopillars are of 1D cone-shaped rod-like morphology, ~50 nm in diameter and ~200 nm in length. The HRTEM image of 400 °C shows that the lattice fringes are about 0.20 nm, which is in good agreement with the interplanar spacing of α-Fe_2O_3 (113) planes. Similarly, the 0.27 nm lattice fringes of 300 °C sample can be attributed to the α-Fe_2O_3 (104) plane. It is worthwhile to mention that diffraction rings of α-Fe_2O_3 become more distinguishable at higher oxidization temperatures (e.g. 400 °C), which is in good agreement with the Raman analysis.

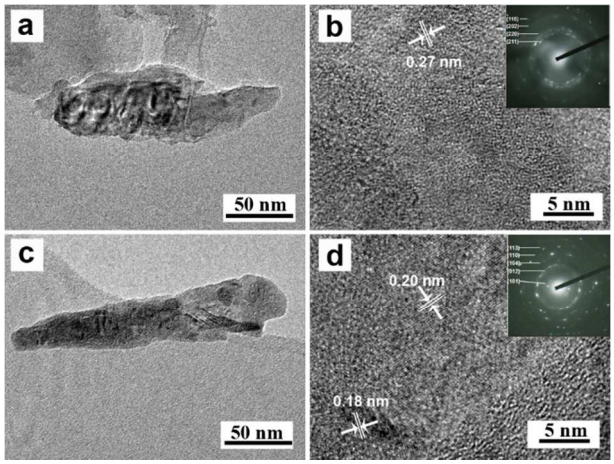

Figure 5. TEM images and HRTEM images: (a) Fe nanopillar oxidized at 300 °C; (b) HRTEM of white box in Figure a, where the inset is the corresponding SAED pattern; (c) Fe nanopillar oxidized at 400 °C; (d) HRTEM of white box in Figure c, where the inset is the corresponding SAED pattern.

PEC experiments were performed to evaluate the photoelectrochemical property of these oxidized samples in a three-electrode cell, using the oxidized samples as the working electrode with an exposed area of 1.5 cm^2 under visible light irradiation. Here 0.01 M KOH aqueous solution was used as the electrolyte. Figure 6(a) shows the photocurrent density measured for these samples with light on and off, at a bias potential of +0.4 V, from which photo-generated electron-hole separation is clearly observed[28]. It can be seen from Figure 6(a) that for samples oxidized at 300, 350 and 400 °C, an increase in the photocurrent was observed for samples. For samples oxidized at >400 °C, i.e., 450 and 500 °C, a monotonic decrease in the photocurrent density was observed. The largest photocurrent density (i.e. 1.4 mA•cm^{-2}) was obtained with the sample oxidized at 400 °C, suggesting a higher efficiency in the separation of electrons and holes and a better photocatalytic activity[29]. Figure 6(b) shows the photocurrent density of the sample oxidized at 400 °C, as a function of time with the light on and off. It can be seen that the photocurrent density is quite stable and repeatable.

Figure 6(c) shows the photocurrent density of these samples measured at various bias potentials ranging from -0.2 V to 0.4 V. The open circuit potential (V_{oc}) relates closely to the difference in the apparent Fermi level between α-Fe_2O_3 and the reference electrode[30], is dependent on the oxidation temperature. From Figure 6(c), it can be seen that the sample oxidized at 400 °C has a minimum of V_{oc} of ~-0.049 V, while the sample oxidized at 500 °C has a maximum value of ~0.183 V. It is well known that a more negative V_{oc} means better electron and hole separation in semiconductors[31-33]. This can be responsible partially for the largest and smallest photocurrent density observed for the two samples.

Table 1 The calculated values of R_s, R_1 and R_{ct} through fitting of the experimental impedance spectra based upon the proposed equivalent circuit in Figure 6(d)

Oxidation Temperature（°C）	300	350	400	450	500
R_s（Ω）	0.52	0.54	0.51	0.51	0.52
C_1（F）	$1.2*10^{-5}$	$3.1*10^{-6}$	$1.9*10^{-6}$	$1.3*10^{-6}$	$1.1*10^{-6}$
R_1（Ω）	31.3	139.7	349.5	431.1	3092
C_2（F）	$8.9*10^{-5}$	$4.6*10^{-5}$	$9.3*10^{-5}$	$8.4*10^{-5}$	$6.7*10^{-5}$
R_{ct}（Ω）	106620	102700	57749	65029	58155

EIS measurements were conducted for all samples at frequencies ranging from 0.1 Hz to100 kHz in 0.01 M KOH electrolyte at open circuit voltage conditions under visible light irradiation. An equivalent circuit was used to fit the Nyquist plots, as shown in Figure 6(d), where the R_s, C_1, R_1, R_{ct}, and C_2 are the series resistance, the capacitance of α-Fe_2O_3 and the electrolyte, the resistance of the holes trapped at surface states, the resistance of holes transferred to the electrolyte through surface states and the capacitance of surface states, respectively. All above values are obtained and listed in Table 1. The specific values of C_1 and C_2 for different oxidation temperatures are basically in the same order of magnitude with little change, respectively. One sees that all samples exhibited a similar R_s with a value around 0.5 Ω. While R_{ct} is normally larger than R_1 two magnitude which indicates the former plays a more important role in circuit. Though values of R_{ct} on 400, 450 and 500 °C are close, R_1 increases from 349.5 to 3092 Ω gradually, which also leads to reduction on photocurrent[34-36]. Based on above analysis it is concluded that the oxidation temperature of 400 °C owns the maximum photocurrent, which is also confirmed by the PEC results.

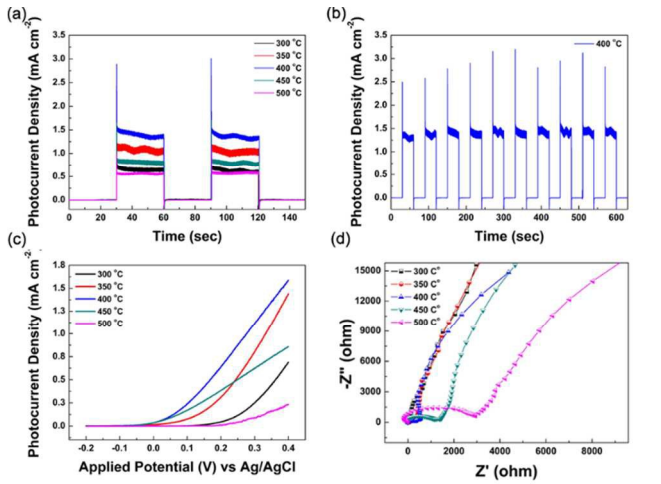

Figure 6. (a) Current versus time measurements of α-Fe_2O_3 at different oxidation temperature during visible light illuminations under 0.4 V versus Ag/AgCl electrode bias. (b) Current versus longer time measurements of α-Fe_2O_3 at 400 °C; (c) *j-V* characteristics of all samples; (d) Nyquist plots under visible light at open circuit voltage of all oxidized sample.

The photoactivities of the obtained α-Fe_2O_3 NPAs are investigated by the degradation of CV with H_2O_2 under visiblelight irradiation, and the degradation processes were tested by recording the characteristic absorbance peak at 584 nm. Figure 7a shows the time course of the decrease in the dye concentration. In absence of α-Fe_2O_3, the CV is degraded by H_2O_2 79.4% until 60 min. While the enhancement is observed after the introduction of α-Fe_2O_3 film; for example, the degradation efficiency of sample oxidized at 400 °C reaches to

90.9% due to the constitution of a Fenton system[37]. After data processing, all reaction follows first-order kinetics as shown in Figure 7b. The rate constant of 400 °C oxidation sample presented by slope is 1.34 times higher than that in absence of α-Fe_2O_3.

According to previous research, α-Fe_2O_3 can be photodecomposed because of the photoreduction of Fe^{3+} to Fe^{2+} under light illumination. Once Fe^{2+} is generated, either it reacts with H_2O_2 generating hydroxy radicals or it detaches from the oxide surface, leaving a vacancy on the semiconductor surface. Once effective collision of dye molecule and the holes happens, CV and/or $CV^{\pm}$ ions form. After the reaction between ions and hydroxyl radicals produced by the decomposition of H_2O_2, CV is degraded completely[38]. The very good photostability of the Fe_2O_3 film strongly suggests that the reaction between surface Fe^{2+} and H_2O_2 is kinetically faster than the Fe^{2+} dissolution reaction in the Fe_2O_3 catalyst surface, thus preventing occurrence of catalyst photocorrosion. We also supplemented experiment choosing methyl orange (MO) as model dye solution (5 μM) in Figure S1, which cannot be degraded under visible lights. According to figure, α-Fe_2O_3 samples with same quantity of H_2O_2 show the similar regular in photocatalysis, in which sample oxidized at 400 °C also shows best degradation performance. And we compare the photocatalytic performance of Fe_2O_3 nanopillar arrays with Fe_2O_3 powders shown in same picture. The sectional view of powder Fe_2O_3 sample is shown in Figure S2.

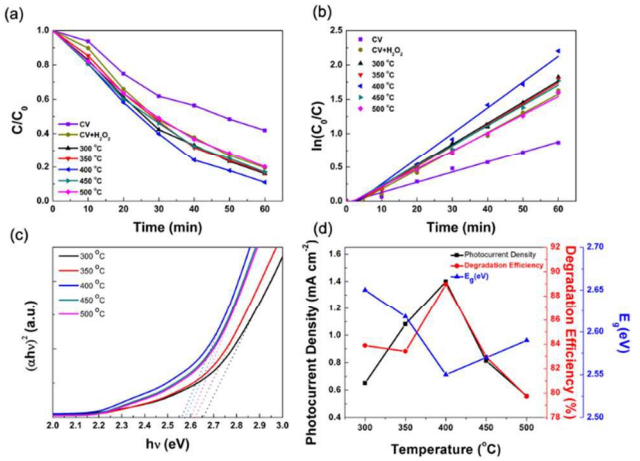

Figure 7. (a) Time course of the decrease in the concentration; (b) $\ln(C_0/C)$ for the degradation of CV with visible irradiation under different conditions; (c) $(\alpha E_{photon})^2$ versus E_{photon} plots of corresponding films; (d) Dependence of photocurrent density, degradation efficiency and bandgap energy on different oxidation temperatures

The band gap energy (E_g) of semiconductor following the equation : $\alpha E_{photon} = K\left(E_{photon} - E_g\right)^{1/2}$, where K, α, E_{photon} and E_g are a constant, the absorption coefficient, the discrete photon energy and the band gap energy, are estimated by calculating the intercept of an extrapolated linear fit to the experimental date of a plot of $(\alpha E_{photon})^2$ *vs* E_{photon} yielded E_g for a direct transition[39] as shown in Figure 7(c). The band gaps of samples from 300 °C to 500 °C are figured out to be 2.27, 2.26, 2.15, 2.16 and 2.18 eV, respectively. It is suggested again that the sample oxidized at 400 °C with narrowest E_g could make more use of light energy as a result of best photocatalytic properties. The change of photocurrent density (under +0.4V bias voltage), degradation efficiency and E_g values over oxidation temperature are summarized in Figure 7 (d) and it is obvious to find 400 °C is the optimal treatment temperature in this system. With the increase of oxidation temperature, grains grow according to the XRD analysis which leads to narrower band gap.[40] However, from XPS analysis in Table 2, with the increase of annealed temperature, oxygen defects on oxide surface becomes less. And this just make semiconductors' band gap become broader.[41] Two opposite factor cause appearance of 400 °C minimum E_g value.

Table 2 Area ratio of oxygen vacancy/oxygen lattice in Figure 8.

Oxidation Temperature（°C）	300	400	500
Area ratio	1.631	1.109	0.650

According to analysis mentioned above, the strong intensity of the Raman peak and small full width at half maximum (FWHM) form progressively with improving oxidation treatment temperature, which means better crystallinity and higher crystallinity can truly enhance the PEC and photodegradation performance of α-Fe_2O_3 nanostructures[31,42,43]. As for why there is an inflexion on property, we look into more information of XPS about oxygen element. The deconvolution peaks display in Figure 8, O 1s spectrum were observed from 529.0 to 536.0 eV. The low binding energy (BE) component observed at ~529 eV corresponds to the main lattice oxygen (O_{lat}) forming oxide with iron. The bands around ~532 eV can be assigned to adsorbed oxygen (O_{ads}) while the peak between them (~521eV) indicates the ionization of oxygen species that could allow compensation for some deficiencies (O_{def}) connected in part to the variations in the concentration of oxygen vacancies in iron oxides[3,44]. Based on Table 2, it is obvious to find the area ratio of oxygen vacancy/oxygen lattice decreases step by step from 1.63 to 0.65 when raising the treatment temperature.

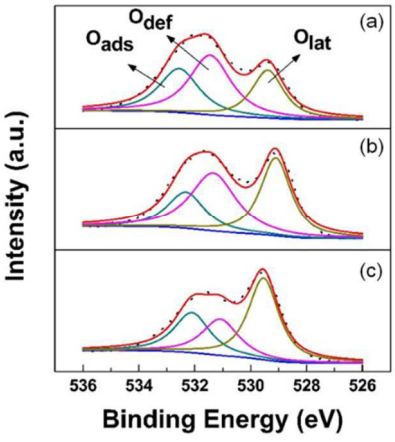

Figure 8. XPS spectra of O 1s of α-Fe_2O_3 oxidized at (a) 300 °C, (b) 400 °C, (c) 500 °C. Red line and black dash lines are the fitted curve and original data, respectively.

Combining former research analysis, oxygen vacancies can trap the photogenerated electrons thus reducing the electron–hole recombination and enhancing photocurrent density and photocatalytic character[45]. When higher oxidation temperature was carried out, the photocatalytic activity of the α-Fe_2O_3 thin films gradually increases due to the improvement of crystallization. However it also reduces oxygen vacancies existing on the surface of oxide, which eventually cuts down active sites and weakens the catalytic performance.

Conclusions

In conclusion, we have introduced the glancing angle e-beam deposition technique with oxidation treatment of vertically aligned α-Fe_2O_3 nanopillars. The PEC and photodegradation properties of samples obtained at different oxidation temperatures from 300 °C to 500 °C are investigated. There are two factors (crystallinity and oxygen vacancies) affect the performances of photocatalyt. With higher oxidation temperature, the improvement of crystallinity will enhance the photocatalytic property while the reduction of oxygen vacancies on the surface of material regarded as photoreaction active sites weakens the performance. The results show that Fe nanopillar arrays oxidized at 400 °C in air demonstrates both the highest photocurrent density (1.4 mA cm^{-2} at 0.4 V vs Ag/AgCl electrode) and the degradation efficiency (90.97 % in 1 hr) on CV in presence of H_2O_2.

Acknowledgments

The authors are grateful to the financial support by the National Natural Science Foundation of China (grant No. 51372135).

Notes and references

[a] School of Materials Science and Engineering, State Key Laboratory of New Ceramics and Fine Processing, Tsinghua University, Beijing 100084, People's Republic of China
[b] School of Materials Science and Engineering, Key Laboratory of Advanced Materials, Tsinghua University, Beijing 100084, People's Republic of China
[c] High-Tech Institute of Xi'an, Xi'an 710025, China

1. A. Fujishima and K. Honda, *Nature*, 1972, **238**, 37-+.
2. K. Sivula, F. Le Formal and M. Gratzel, *Chemsuschem*, 2011, **4**, 432-449.
3. S. M. Park, T. Ikegami and K. Ebihara, *Thin Solid Films*, 2006, **513**, 90-94.
4. X. Wang, J. Wang, Z. Cui, S. Wang and M. Cao, *Rsc Adv*, 2014, **4**, 34387-34394.
5. S. A. Jadhav, R. Bongiovanni, D. L. Marchisio, D. Fontana and C. Egger, *Pigm Resin Technol*, 2014, **43**, 219-227.
6. Y. V. Kaneti, Q. M. D. Zakaria, Z. Zhang, C. Chen, J. Yue, M. Liu, X. Jiang and A. Yu, *J Mater Chem A*, 2014, **2**, 13283-13292.
7. T. W. Hamann, *Dalton T*, 2012, **41**, 7830-7834.
8. Z. J. Zhang, B. Q. Wei and P. M. Ajayan, *Appl Phys Lett*, 2001, **79**, 4207-4209.
9. R. H. Wang, C. H. Xu, J. Sun and L. Gao, *Sci Rep-Uk*, 2014, **4**.
10. K. Nagato, M. Furubayashi, T. Hamaguchi and M. Nakao, *Microelectron Eng*, 2011, **88**, 2697-2699.
11. Y. L. Cheng, B. L. Zou, C. J. Wang, Y. J. Liu, X. Z. Fan, L. Zhu, Y. Wang, H. M. Ma and X. Q. Cao, *Crystengcomm*, 2011, **13**, 2863-2870.
12. K. Woo, H. J. Lee, J. P. Ahn and Y. S. Park, *Adv Mater*, 2003, **15**, 1761-+.
13. Z. Liu, B. L. Lv, D. Wu, Y. H. Sun and Y. Xu, *Particuology*, 2013, **11**, 327-333.
14. Q. Wei, Z. C. Li, Z. J. Zhang and Q. Zhou, *Mater Trans*, 2009, **50**, 1351-1354.
15. W. H. Peng, C. L. Zhu, S. M. Zhu, F. Yao, Y. Li and D. Zhang, *J Mater Sci*, 2013, **48**, 4336-4344.
16. H. Dotan, K. Sivula, M. Gratzel, A. Rothschild and S. C. Warren, *Energ Environ Sci*, 2011, **4**, 958-964.
17. B. M. Klahr and T. W. Hamann, *J Phys Chem C*, 2011, **115**, 8393-8399.
18. Z. Yang, J. Xu, C. Wu, H. Jing, P. Li and H. Yin, *Applied Catalysis B: Environmental*, 2014, **156–157**, 249-256.
19. C. Q. Zhu, Y. R. Li, Q. Su, B. A. Lu, J. Q. Pan, J. W. Zhang, E. Q. Xie and W. Lan, *J Alloy Compd*, 2013, **575**, 333-338.
20. Q. Y. Hao, S. A. Liu, X. M. Yin, Z. F. Du, M. Zhang, L. M. Li, Y. G. Wang, T. H. Wang and Q. H. Li, *Crystengcomm*, 2011, **13**, 806-812.
21. A. J. R. Hensley, Y. C. Hong, R. Q. Zhang, H. Zhang, J. M. Sun, Y. Wang and J. S. McEwen, *Acs Catal*, 2014, **4**, 3381-3392.
22. Q. Wei, Z. J. Zhang, Z. C. Li, Q. Zhou and Y. Zhu, *J Phys D Appl Phys*, 2008, **41**.
23. A. A. Tahir, K. G. U. Wijayantha, S. Saremi-Yarahmadi, M. Mazhar and V. Mckee, *Chem Mater*, 2009, **21**, 3763-3772.
24. D. Bersani, P. P. Lottici and A. Montenero, *J Raman Spectrosc*, 1999, **30**, 355-360.
25. S. H. Huang and J. Liu, *Chinese Phys B*, 2014, **23**.
26. J. S. Xu and Y. J. Zhu, *Crystengcomm*, 2012, **14**, 2702-2710.
27. T. Fujii, F. M. F. de Groot, G. A. Sawatzky, F. C. Voogt, T. Hibma and K. Okada, *Phys Rev B*, 1999, **59**, 3195-3202.
28. Q. Kang, J. Y. Cao, Y. J. Zhang, L. Q. Liu, H. Xu and J. H. Ye, *J Mater Chem A*, 2013, **1**, 5766-5774.
29. Y. Liu, C. S. Xie, J. Li, T. Zou and D. W. Zeng, *Appl Catal a-Gen*, 2012, **433**, 81-87.
30. D. R. Baker and P. V. Kamat, *Adv Funct Mater*, 2009, **19**, 805-811.
31. Z. Xie, X. X. Liu, W. P. Wang, X. J. Wang, C. Liu, Q. Xie, Z. C. Li and Z. J. Zhang, Nano Energy, 2015, 11, 400-408.
32. M. Jakob, H. Levanon and P. V. Kamat, *Nano Lett*, 2003, **3**, 353-358.
33. A. Wood, M. Giersig and P. Mulvaney, *J Phys Chem B*, 2001, **105**, 8810-8815.
34. J. C. Chou, S. A. Lin, C. Y. Lee and J. Y. Gan, *J Mater Chem A*, 2013, **1**, 5908-5914.
35. Y. Hou, F. Zuo, A. Dagg and P. Y. Feng, *Nano Lett*, 2012, **12**, 6464-6473.
36. K. Y. Yoon, J. S. Lee, K. Kim, C. H. Bak, S. I. Kim, J. B. Kim and J. H. Jang, *Acs Appl Mater Inter*, 2014, **6**, 22634-22639.
37. B. Xu, B. B. Huang, H. F. Cheng, Z. Y. Wang, X. Y. Qin, X. Y. Zhang and Y. Dai, *Chem Commun*, 2012, **48**, 6529-6531.
38. H. Xie, Y. Z. Li, S. F. Jin, J. J. Han and X. J. Zhao, *J Phys Chem C*, 2010, **114**, 9706-9712.
39. L. Xu, J. X. Xia, L. G. Wang, J. Qian, H. M. Li, K. Wang, K. Y. Sun and M. Q. He, *Chem-Eur J*, 2014, **20**, 2244-2253.
40. J. G. Yu, H. G. Yu, B. Cheng, X. J. Zhao, J. C. Yu and W. K. Ho, *J Phys Chem B*, 2003, **107**, 13871-13879.
41. P. Zhan, Z. Xie, Z. C. Li, W. P. Wang, Z. J. Zhang, Z. X. Li, G. D. Cheng, P. Zhang, B. Y. Wang and X. Z. Cao, *Appl Phys Lett*, 2013, **102**
42. R. Rajendran, Z. Yaakob, M. Pudukudy, M. S. A. Rahaman and K. Sopian, *J Alloy Compd*, 2014, **608**, 207-212.
43. P. M. Kouotou, Z. Y. Tian, H. Vieker, A. Beyer, A. Golzhauser and K. Kohse-Hoinghaus, *J Mater Chem A*, 2013, **1**, 10495-10504.

44. J. C. Dupin, D. Gonbeau, P. Vinatier and A. Levasseur, *Phys Chem Chem Phys*, 2000, **2**, 1319-1324.
45. R. Lv, T. Wang, F. L. Su, P. Zhang, C. J. Li and J. L. Gong, *Nano Energy*, 2014, **7**, 143-150.

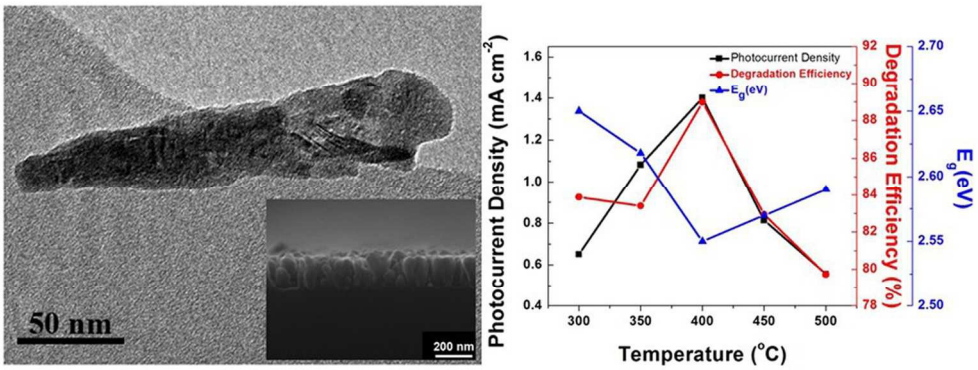

396x158mm (96 x 96 DPI)